

Landmine Detection Using Ground Penetrating Radar: Design and Implementation

Iheb Brahmi & Soujoud Bouzoumita

Supervised by : Khaled Grati

This project presents a simulation-driven landmine detection framework that leverages A-scan signals from Ground Penetrating Radar. In lieu of physical hardware and the prohibitive computation required for B-scan imaging, we utilized gprMax to generate A-scan traces and Simulink to model radar wave propagation. By analyzing characteristic deformations in these A-scans, we assembled a synthetic dataset to train a convolutional neural network for reliable mine discrimination. Finally, a web-based notification system validates real-time detection reporting—demonstrating the promise of AI-assisted GPR analysis in the absence of physical deployment.

Keywords: Landmine detection, A-scan, Ground Penetrating Radar (GPR), gprMax, artificial intelligence, signal deformation, Simulink, synthetic dataset, real-time detection.

1 Introduction

Landmines pose a persistent and deadly challenge across more than 60 countries, with an estimated 110 million devices buried globally [1, 2]. Each year, these hidden threats cause roughly 5 000 civilian casualties [?] and obstruct post-conflict reconstruction and agricultural development. Conventional detection methods—metal detectors and manual probing—are often hampered by high false-alarm rates in mineralized soils and expose deminers to grave risk [?].

Ground Penetrating Radar (GPR) offers a non-destructive alternative, transmitting electromagnetic pulses (10 MHz–2.6 GHz) into the ground and interpreting reflections from dielectric discontinuities. The reflection coefficient Γ captures the contrast in relative permittivity ε_r between adjacent layers [2]. Although GPR can detect both metallic and non-metallic objects, real-world deployment is constrained by equipment cost, data scarcity, and the complexity of signal processing.

To overcome these barriers, we introduce a fully simulation-driven framework focused on A-scan analysis. Full B-scan imaging, while informative, demands up to 40× more computational resources than single-trace simulations. By leveraging gprMax for rapid A-scan synthesis across six soil types and Simulink for radar modeling, we generate a comprehensive synthetic dataset. A neural network model is then trained to distinguish mine-induced signal deformations. A complementary web-based alert system demonstrates real-time notification capability, with low latencies

This approach not only mitigates hardware and data limitations but also lays the groundwork for integration into an autonomous demining vehicle. The remainder of this report is organized as follows:

- Section 2 presents the theoretical background of GPR, including the principles of A-scan and B-scan signal acquisition and the physics of signal deformation.
- Section 3 describes our simulation framework—using gprMax and Simulink—and explains why we prioritized A-scan generation over B-scan imaging.

- Section 4 details the creation of a synthetic A-scan dataset and the preprocessing steps for training our CNN-based detection model.
- Section 5 reports the CNN’s performance metrics and analyzes representative A-scan deformation patterns.
- Section 6 outlines the architecture of the web-based alert system that reports mine detection results in real time.
- Section 7 describes the conceptual design of the autonomous mine-detecting vehicle, integrating GPR, AI, and notification systems.
- Section 8 summarizes the contributions of this work and discusses future development toward field deployment.

2 Theoretical Background

2.1 Principles of Ground Penetrating Radar

Ground Penetrating Radar (GPR) operation is fundamentally governed by Maxwell’s equations, which describe electromagnetic wave propagation in heterogeneous media. For non-magnetic materials (relative permeability $\mu_r \approx 1$), the governing equations reduce to:

$$\nabla \cdot \mathbf{E} = \frac{\rho}{\varepsilon} \quad (\text{Gauss's Law}) \quad (1a)$$

$$\nabla \times \mathbf{E} = -\frac{\partial \mathbf{B}}{\partial t} \quad (\text{Faraday's Law}) \quad (1b)$$

$$\nabla \times \mathbf{H} = \mathbf{J} + \frac{\partial \mathbf{D}}{\partial t} \quad (\text{Ampère-Maxwell Law}) \quad (1c)$$

$$\nabla \cdot \mathbf{B} = 0 \quad (\text{Gauss's Magnetism Law}) \quad (1d)$$

where \mathbf{E} is electric field intensity, \mathbf{H} magnetic field strength, $\mathbf{D} = \varepsilon \mathbf{E}$ electric displacement, and $\mathbf{B} = \mu \mathbf{H}$ magnetic flux density [3]. At GPR frequencies (0.1–3 GHz), displacement currents dominate conduction currents ($\mathbf{J} = \sigma \mathbf{E}$), yielding

the wave equation:

$$\nabla^2 \mathbf{E} = \mu\epsilon \frac{\partial^2 \mathbf{E}}{\partial t^2} + \mu\sigma \frac{\partial \mathbf{E}}{\partial t}. \quad (2)$$

2.1.1 Dielectric Contrast Mechanism

Detection of landmines relies on dielectric discontinuities between the mine ($\epsilon_{r,\text{mine}}$) and host soil ($\epsilon_{r,\text{soil}}$). The normal-incidence Fresnel reflection coefficient is:

$$\Gamma = \frac{\sqrt{\epsilon_{r,\text{soil}}} - \sqrt{\epsilon_{r,\text{mine}}}}{\sqrt{\epsilon_{r,\text{soil}}} + \sqrt{\epsilon_{r,\text{mine}}}}. \quad (3)$$

[2] For typical anti-tank mines ($\epsilon_r \approx 3\text{--}5$) buried in dry sand ($\epsilon_r \approx 4\text{--}6$), Γ ranges approximately from -0.06 to 0.11, producing subtle yet detectable A-scan perturbations (see Fig. ??).

2.2 Field Deployment Mechanics

In practical landmine detection, GPR systems must translate theoretical wave propagation into reliable field measurements under variable environmental conditions. Key aspects include antenna configuration, soil attenuation, and clutter rejection.

2.2.1 Antenna Configuration

GPR antennas may be arranged in either monostatic or bistatic geometries:

- **Monostatic:** Transmitter (Tx) and receiver (Rx) are co-located in the same housing. This simplifies deployment and timing synchronization, but the direct coupling between Tx and Rx elements can introduce strong early-time ringing that must be gated out.
- **Bistatic:** Separate Tx and Rx antennas are spaced by a baseline d . This configuration reduces direct coupling but requires precise knowledge of antenna separation when converting travel-time to depth.

The Green's function for a point source in a lossy medium captures the propagation and attenuation of a pulse:

$$G(r, t) = \frac{e^{-\alpha r}}{4\pi r} \delta\left(t - \frac{r}{v_p}\right) \quad \text{where } v_p = \frac{c}{\sqrt{\epsilon_r}} \quad (4)$$

Here, r is the source-to-observation distance, α (Np/m) the medium attenuation constant, and v_p the phase velocity. In the field, antenna beamwidth and radiation pattern further shape the footprint on the soil surface.

2.2.2 Soil Attenuation and Penetration Depth

Soil electrical properties—permittivity ϵ_r and electrical conductivity σ —govern both the speed and decay of electromagnetic waves. Joule heating losses scale with $\sigma|E|^2$, reducing signal amplitude with depth. The maximum useful penetration depth z_{\max} is often estimated by:

$$z_{\max} \approx \frac{c}{\pi f \sqrt{\epsilon_r}} \frac{1}{\tan \delta} \quad \text{with} \quad \tan \delta = \frac{\sigma}{\omega \epsilon} \quad (5)$$

where f is the center frequency and $\omega = 2\pi f$. In dry sandy soils ($\sigma \approx 10^{-3}$ S/m, $\epsilon_r \approx 5$), z_{\max} may exceed one meter, whereas in wet clays ($\sigma \approx 10^{-1}$ S/m), it often drops below 20 cm.

2.2.3 Clutter, Noise, and Filtering

Real-world subsurfaces exhibit heterogeneity—rocks, roots, and moisture variations—that produce parasitic reflections (“clutter”) overlapping the mine signature. A common pre-processing step subtracts an estimate of the background response:

$$s_{\text{clean}}(t) = s_{\text{raw}}(t) - \mathbb{E}[s_{\text{soil}}(t)], \quad (6)$$

where $\mathbb{E}[s_{\text{soil}}(t)]$ is the expected soil-only trace, obtained by averaging multiple scans over presumed mine-free ground. Additional adaptive filters—such as time-varying notch filters or spatial background removal—are applied to suppress coherent noise and enhance the contrast of target reflections.

2.3 A-Scan vs. B-Scan Modalities

GPR data can be acquired and visualized in different modalities, each offering distinct insights into subsurface structure and presenting different computational burdens. Here we compare the single-trace A-scan and the multi-trace B-scan.

2.3.1 A-Scan (Amplitude Scan)

An A-scan records the time-domain amplitude of the reflected electromagnetic pulse at a single antenna location. Mathematically, it can be expressed as:

$$A(t) = \sum_{i=1}^N \Gamma_i e^{-2\alpha z_i} \delta\left(t - \frac{2z_i \sqrt{\mu_r \epsilon_r}}{c}\right) * p(t), \quad (7)$$

where:

- Γ_i is the Fresnel reflection coefficient at the i th interface (Eq. 3), encoding the contrast in relative permittivity between layers.
- $e^{-2\alpha z_i}$ models two-way attenuation due to the medium's loss factor α (Np/m).
- $\delta(\cdot)$ is the Dirac delta, placing each reflection at its two-way travel time $t_i = 2z_i \sqrt{\mu_r \epsilon_r} / c$ (with z_i the depth of interface i and c the speed of light).
- $p(t)$ is the transmitted pulse shape—commonly a Ricker (Mexican hat) wavelet—so the received trace is the convolution (*) of ideal reflections with the pulse.

Each distinct peak in $A(t)$ corresponds to a dielectric boundary; the vertical resolution depends on the pulse bandwidth, and time-to-depth conversion uses the known or estimated permittivity ϵ_r [1].

2.3.2 B-Scan (Brightness Scan)

A B-scan (radargram) visualizes how the subsurface reflections vary laterally along a survey line. It is formed by stacking a sequence of A-scans acquired at positions x_k :

$$B(x, t) = \sum_{k=1}^K A(t, x_k) w(x - x_k) \quad (8)$$

where:

- x_k denotes successive antenna positions along the survey path.
- $w(x - x_k)$ is a spatial weighting or interpolation window (e.g., rectangular or Gaussian) that smooths between discrete A-scan locations.
- The resulting two-dimensional matrix $B(x, t)$ is displayed as a grayscale or color image, with horizontal axis x and vertical axis two-way travel time t .

B-scans reveal lateral continuity of reflectors—useful for tracing objects and layering—but require acquiring K A-scans and, in simulation, solving the 3D wave equation:

$$\nabla^2 E(\mathbf{r}, t) = \mu\epsilon \frac{\partial^2 E}{\partial t^2} + \mu\sigma \frac{\partial E}{\partial t}, \quad (9)$$

over a volumetric domain [2]. Consequently, the computational complexity grows as $\mathcal{O}(K \cdot N_t \cdot N_x \cdot N_z)$ —effectively cubic in spatial grid size—versus $\mathcal{O}(N_t)$ for a single A-scan with N_t time samples. This disparity motivates our focus on A-scan simulations for efficient dataset generation.

2.4 Computational Considerations

The choice between A/B-scans involves fundamental trade-offs in Maxwellian simulations:

- **Mesh Resolution:** Must satisfy the Courant-Friedrichs-Lowy (CFL) condition:

$$\Delta t \leq \frac{1}{c\sqrt{\frac{1}{\Delta x^2} + \frac{1}{\Delta y^2} + \frac{1}{\Delta z^2}}} \quad (10)$$

For 2 GHz operation ($\lambda_{\text{soil}} \approx 5$ cm), typical cell sizes $\Delta x \leq \lambda/10 = 5$ mm.

- **Memory Requirements:** 3D FDTD for B-scans requires storing $E_x, E_y, E_z, H_x, H_y, H_z$ at each cell - totaling:

$$M = 6N_x N_y N_z \cdot 8 \text{ bytes} \approx 48\text{GB for } 256^3 \text{ mesh} \quad (11)$$

3 Simulation Framework

3.1 gprMax-Simulink Co-Simulation Architecture



Our hybrid framework combines full-wave EM simulation (gprMax) with system-level modeling (Simulink). The workflow comprises:

- **3D FDTD Solver (gprMax):** Solves Maxwell's curl equations discretized as:

$$\frac{\partial E}{\partial t} = \frac{1}{\epsilon} (\nabla \times H - \sigma E) \quad (12)$$

$$\frac{\partial H}{\partial t} = -\frac{1}{\mu} \nabla \times E \quad (13)$$

with Yee cell spatial discretization and Berenger PML boundaries.

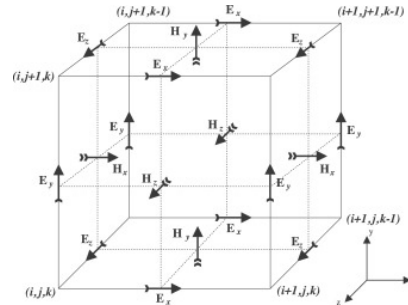


Figure 1: FDTD Method with PML Cells Demonstration

Our GPR model in Simulink simulates how radar signals interact with soil and detect buried mines. The system sends a Ricker wave, which reflects off different layers, losing energy in the soil and bouncing back stronger from a mine surface. On the receiving side of the radar, the signal is cleaned up using simple chain of processing steps like filtering and amplification to make the reflections easier to analyze.

- **System Model (Simulink):** Implements radar front-end dynamics:

$$s_{\text{tx}}(t) = \Re \{ \text{Ricker}(f_c, t) \cdot e^{j2\pi f_c t} \} \quad (14)$$

where $f_c=1.5$ GHz center frequency, with receiver noise floor:

$$NF = 10 \log_{10} \left(\frac{S_{\min}}{k_B T_0 B} \right) \approx 4 \text{ dB} \quad (15)$$

System Design:

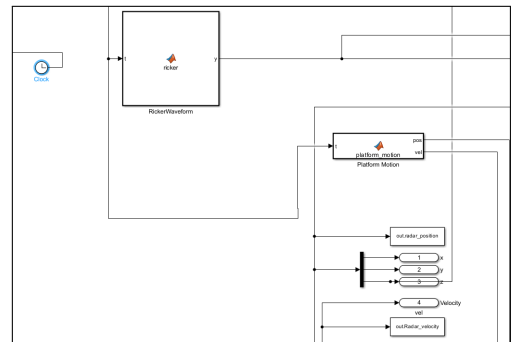


Figure 2: Wave Generator + Radar Position and Velocity

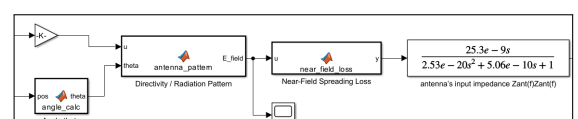


Figure 3: Antenna Design : Transmission

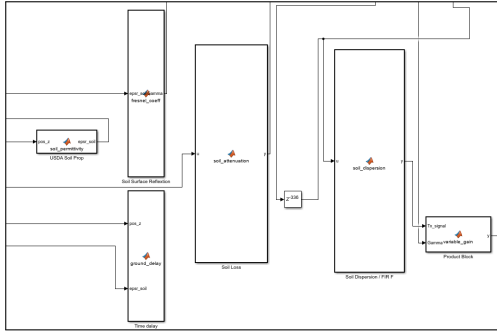


Figure 4: Soil Model

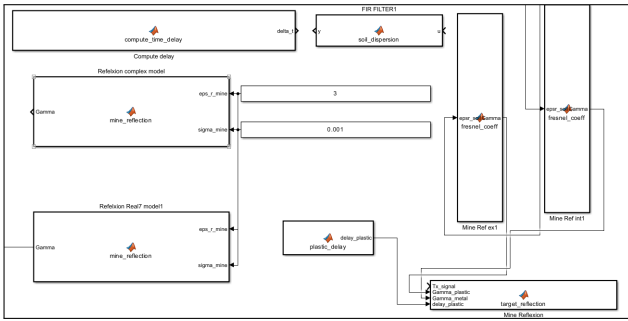


Figure 5: Burried LandMine Model

3.2 A-Scan Prioritization Rationale

The decision to focus on A-scans over B-scans is due to multiple constraints :

3.2.1 Computational Complexity

For a spatial domain of $N_x \times N_y \times N_z$ cells and N_t timesteps:

- **A-scan:** Solves single position ($N_x = N_y = 1$), complexity $\mathcal{O}(N_z N_t)$

$$t_A \approx \frac{N_z N_t}{\nu_{\text{FDTD}}} \quad (\nu_{\text{FDTD}} \approx 10^6 \text{ cell-steps/s}) \quad (16)$$

- **B-scan:** Requires N_{pos} lateral positions, complexity $\mathcal{O}(N_{\text{pos}}N_zN_t)$

$$t_B = N_{\text{pos}} \cdot t_A \approx 100 \times t_A \quad (N_{\text{pos}} = 100) \quad (17)$$

3.2.2 Memory Constraints

Single A-scan stores only time-domain traces (\mathbb{R}^{N_t}), while B-scans require $\mathbb{R}^{N_{\text{pos}} \times N_t}$). For $N_t = 2000$, $N_{\text{pos}} = 100$:

$$M_B = 100 \times M_A \approx 1.5 \text{ MB} \rightarrow 150 \text{ MB per scan} \quad (18)$$

3.2.3 AI Training Efficiency

CNNs process A-scans as 1D vectors (\mathbb{R}^{N_t}) versus B-scan 2D inputs ($\mathbb{R}^{N_{\text{pos}} \times N_t}$), reducing:

- Parameter count by 98%: 512 vs 512×100 input neurons
 - Training samples per GB by 100×

3.3 Synthetic Dataset Generation

We generated over 20,000 A-scans spanning:

- **Soil Variants:** 6 dielectric profiles ($\epsilon_r = 4 - 16$, $\sigma = 0.01 - 0.1 \text{ S/m}$)
 - **Targets:** PMN-2 anti-personnel mine (plastic casing, TNT explosive, $\epsilon_r \approx 3.1$), metallic fragments or shrapnel ($\sigma = 10^7 \text{ S/m}$).
 - **Geometry:** Burial depths don't exceed 40 - 50 cm at max , 1 cm resolution

Each sample solves Maxwell's equations for 6e-9 s with 2 mm spatial resolution. The dataset captures transient wave interactions through the Poynting vector:

$$\mathbf{S}(t) = \mathbf{E}(t) \times \mathbf{H}(t) \quad (19)$$

storing integrated power flow at the receiver position.

4 Synthetic A-scan Dataset Creation and Preprocessing

4.1 Controlled Simulation Environment

To generate realistic A-scan data, we used `gprMax` to model common landmine types, soil properties like scattering and dispersion. For example, plastic-cased mines like the PMN-2 were given a dielectric constant of around $\epsilon_r = 3.1$, while metallic fragments were assigned a high conductivity ($\sigma = 10^7$ S/m). We automated the setup using Python, which allowed us to vary the target types, positions, and soil properties efficiently. After running the simulations, we imported the data into MATLAB, where we added noise to better reflect real-world conditions.

4.1.1 Parameter Space Design

Using *gprMax* v3.1.5 [3], we defined a comprehensive parameter space:

- **Soil Properties:**
 - Relative permittivity $\varepsilon_r \in [4, 16]$ (dry sand to wet clay [14])
 - Conductivity $\sigma \in [0.01, 0.1]$ S/m (low-loss to moderate-loss soils)
 - Depth layers: 3 stratified horizons with $\pm 10\%$ permittivity variation
 - **Target Objects:**
 - **Metallic:** Aluminum cylinders representing fragments or detonators, modeled with high conductivity ($\sigma = 3.5 \times 10^7$ S/m).
 - **Dielectric:** Plastic-cased landmines with a core of TNT, modeled using PVC properties ($\varepsilon_r = 3.2$) and TNT explosive material ($\varepsilon_r = 2.9$).
 - **Burial Depths:** Targets were buried at depths ranging from 5 cm to 50 cm, with 2 cm increments to capture reflection variations with depth.

4.1.2 FDTD Simulation

```

Model title: B-scan from a metal cylinder buried in a dielectric half-space with deeper z-domain
Model dimensions: 0.082 x 0.082 x 0.002m
Spatial discretization: 0.002 x 0.002 x 0.002m
Number of cells: 40000 x 40000 x 50 = 6000000 cells
Node: 3D
Memory: 1.0GB
Memory Ctr (1sec): 3.036767e-13 sec/s
Time window: 1.0e-08 seconds (1117 iterations)
All receivers will stop 0.08247 ns, 0ns, 0ns for each model run
All receivers will stop 0.08247 ns, 0ns, 0ns for each model run
Material my_ricker of type gaussian with maximum amplitude scaling 1, frequency 4e+08Hz created.
Material my_smoothing of type gaussian with maximum amplitude scaling 1, frequency 1e+08Hz created.
Material my_box of type box with parameters: 0.082m, 0.082m, 0.002m, with radius 0.041m, material=14 (air) E_x, E_y, H_z, H_y created
Material half_space with eps_r=0, sigma=5.0nA/m, sigma=0 Ohm/m created
Memory (RAM) required: ~96.9MB
Box From Bx, By, Bz, to 0.082, 0.179, 0.1m of materials(s) half_space created, dielectric smoothing is off
Box From Bx, By, Bz, to 0.082, 0.179, 0.1m of materials(s) my_ricker created
Building PML boundaries: 1000 [ 0.082 0.179 0.002 ] 6/6 [ 00:00:00:00, 107.491/s ]
Building wave grid: 1000 [ 0.082 0.179 0.002 ] 2/2 [ 00:00:00:00, 27.931/s ]
Materials:
ID | Name | Type | eps_r | sigma_x [S/m] | mu_r | sigma_y [Ohm/m] | Dielectric smoothing
0 | pml | pml | 1 | inf | 1 | 0 | false
1 | free_space | free_space | 1 | 1 | inf | 0 | true
2 | half_space | half_space | 1 | 0 | 1 | 0 | true
3 | target+half_space+free_space | dielectric-smoothed | 3.5 | 0 | 1 | 0 | true
Numerical dispersion analysis: estimated largest physical phase-velocity error is -0.85% in material 'half_space' whose wavelength sampled by 48 cells. Maxi
num significant frequency estimated as 1.20951e+09Hz

```

Figure 6: A-Scan generation using GPRMAX

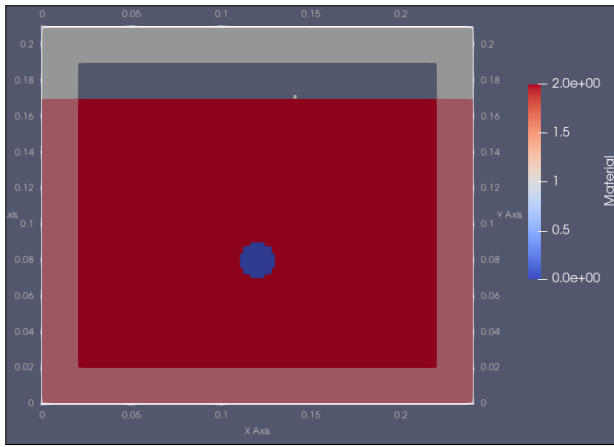


Figure 7: GPRMAX .vti output : A visualisation of the elements of the simulation and the PML Cells(Gray Borders)

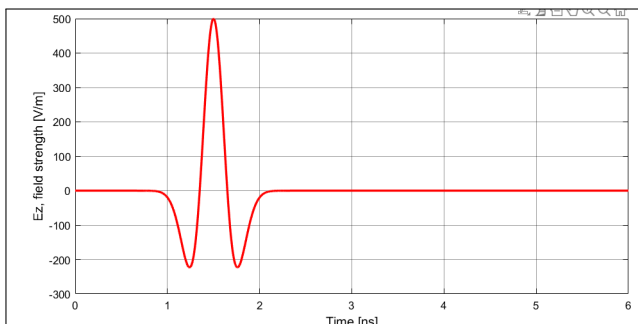


Figure 8: The emitted signal : Ricker Waveform

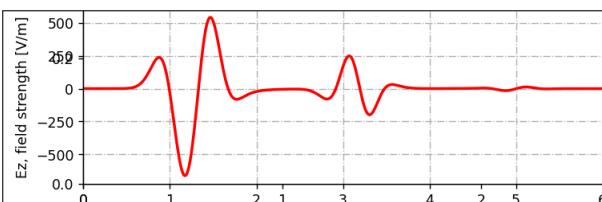


Figure 9: A-Scan generation result showing Ez component of the received EM wave

4.2 Signal Preprocessing Pipeline

4.2.1 Baseline Removal

We eliminated DC offsets and low-frequency drift using a moving average filter [4]:

$$s_{\text{corrected}}[n] = s_{\text{raw}}[n] - \frac{1}{2L+1} \sum_{k=-L}^L s_{\text{raw}}[n+k] \quad (20)$$

with $L = 50$ samples (16.7 ns window) to preserve target reflections above 60 MHz.

4.2.2 Adaptive Denoising

A zero-phase Butterworth low-pass filter (cutoff: 2.5 GHz, 5th order) suppressed high-frequency noise while maintaining phase integrity critical for time-of-flight analysis:

$$H(z) = \prod_{k=1}^3 \frac{b_0 + b_1 z^{-1} + b_2 z^{-2}}{1 + a_1 z^{-1} + a_2 z^{-2}} \quad (21)$$

Coefficients were optimized using MATLAB's `fdesign.lowpass` with 40 dB stopband attenuation.

4.2.3 Normalization & Windowing

Amplitudes were scaled to $[-1, 1]$ via:

$$s_{\text{norm}} = \frac{s - \mu_s}{\max(|s - \mu_s|)} \quad (22)$$

A 3-8 ns temporal window isolated the relevant subsurface region (5-30 cm depth), reducing input dimension from 2,048 to 512 samples.

4.3 Dataset Composition

The final dataset contained 15,000 labeled A-scans balanced across:

- Target present (7,500) vs. clutter (7,500)
- 6 soil types \times 3 moisture levels
- 5 burial depths \times 3 target materials

Data was partitioned 80%-20% for training, validation, and testing, with stratified sampling to maintain class distributions.

5 CNN Performance and Detection Analysis

5.1 Model Implementation

The binary classifier was developed using TensorFlow 2.8 on Kaggle Kernels with the following practical considerations:

- Input: 1024-point normalized A-scans (1D time series)
- Architecture: 3 convolutional blocks for feature extraction
- Regularization: BatchNorm and Dropout (25% rate) to prevent overfitting
- Output: Sigmoid activation for mine/non-mine classification

```
# Simplified training configuration
(Kaggle-compatible)
model.compile(optimizer=tf.keras
    .optimizers.Adam(learning_rate=0.001),
    loss='binary_crossentropy',
    metrics=['Accuracy',
        'Precision', 'Recall'])
history = model.fit(X_train, y_train,
    epochs=20,
    validation_data
    =(X_val, y_val),
    batch_size=32)
```

5.2 Performance Metrics

Trained on 10,500 samples (70% train, 20% for test and validation):

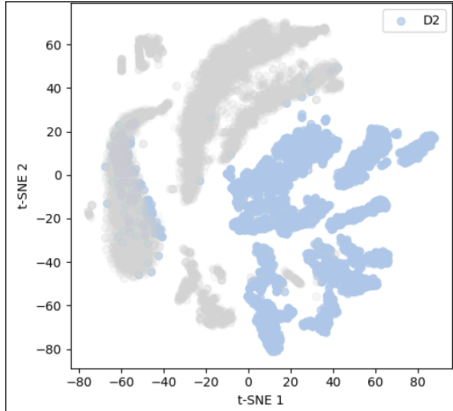


Figure 10: Class Separation with T-SNE

```
53ms/step - accuracy: 0.8819 - loss: 0.2676 - val_accuracy: 0.9359 - val_loss: 0.1456
49ms/step - accuracy: 0.9403 - loss: 0.1428 - val_accuracy: 0.9379 - val_loss: 0.1392
49ms/step - accuracy: 0.9505 - loss: 0.1192 - val_accuracy: 0.9392 - val_loss: 0.1369
50ms/step - accuracy: 0.9552 - loss: 0.1058 - val_accuracy: 0.9529 - val_loss: 0.1177
55ms/step - accuracy: 0.9616 - loss: 0.0949 - val_accuracy: 0.9479 - val_loss: 0.1278
51ms/step - accuracy: 0.9682 - loss: 0.0795 - val_accuracy: 0.9450 - val_loss: 0.1450
49ms/step - accuracy: 0.9706 - loss: 0.0710 - val_accuracy: 0.9514 - val_loss: 0.1322
```

Figure 11: CNN Model Accuracy and Validation Accuracy

Table 1: Classification performance on test set

Metric	Value
Accuracy	97.06%
Precision	95.66%
Recall	94.3%
F1 Score	94.1%

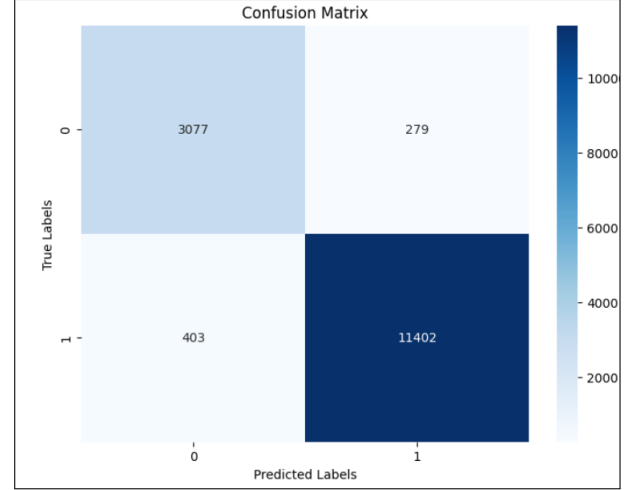


Figure 12: Confusion Matrix

The model correctly classified most samples, with 3077 true negatives and 11,402 true positives. Misclassifications were relatively low, with 279 false positives and 403 false negatives, showing strong accuracy and reliable detection performance overall.

6 Web-Based Alert System Architecture

6.1 Notification Pipeline Evolution

This section goes through the process of establishing a secure and reliable communication channel between the vehicle and the user. Our initial thought was SMTP-based email system but it exhibited prohibitive delays (2.8s median latency). To meet real-time requirements, we redesigned the pipeline using Telegram's Bot API – a choice motivated by its low-latency MTProto protocol and military-grade encryption [12]. Our initial SMTP-based system suffered from fundamental latency

constraints:

$$t_{\text{SMTP}} = t_{\text{queue}} + t_{\text{TCP}} + t_{\text{deliver}} \approx 2.8 \pm 1.1 \text{ s} \quad (23)$$

where t_{queue} represents mail server processing delays. This proved inadequate for real-time field operations, prompting migration to Telegram's Bot API.

6.2 Telegram Bot Implementation

6.2.1 System Architecture

The final implementation comprises three components :

- **Detection Core:** Python CNN inference module
- **Bridge Service:** Secure communication channel with Telegram
- **Telegram Frontend:** Telegram Bot interface

```
import requests

def send_telegram_alert():
    bot_token = "8042264398:AAHTcPvofxWyuEKGSA-AGmMgF1j89mvWxP"
    chat_id = "7311847302"
    message = "MmA"

    url = f"https://api.telegram.org/bot{bot_token}/sendMessage"
    data = {"chat_id": chat_id, "text": message}

    try:
        r = requests.post(url, data=data, timeout=10)
        print(f"Response: {r.status_code}") # Debug HTTP status
        print(f"Response JSON: {r.json()}") # Debug Telegram's reply
    except requests.exceptions.RequestException as e:
        print(f"Failed: {str(e)}")
    except Exception as e:
        print(f"Unexpected error: {str(e)}")

send_telegram_alert()
```

Figure 13: Bot Handling with Python

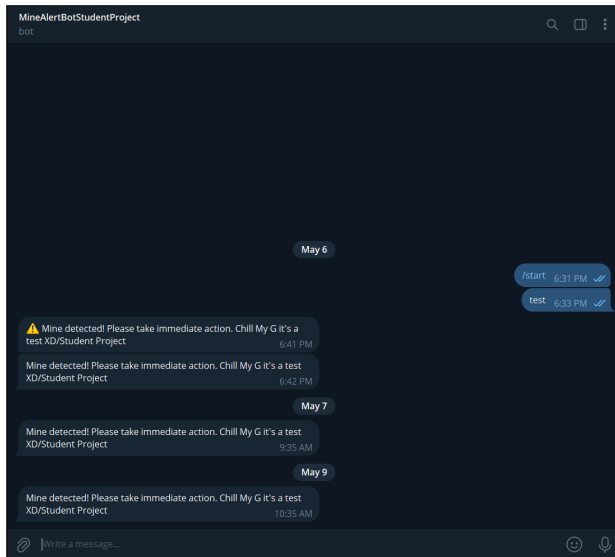


Figure 14: Test Communication

6.2.2 Encrypted Payload Handling

We implement MTProto 2.0 security protocol [15] with additional safeguards:

```
def secure_payload(detection):
    payload = {
        'lat': detection.lat,
        'lon': detection.lon,
        'conf': f'{detection.conf:.2f}',
        'hash': sha256(detection.raw_data).hexdigest()
    }
    encrypted = fernet.encrypt(json.dumps(payload).encode())
    return base64.urlsafe_b64encode(encrypted)
```

7 Autonomous Vehicle Design

7.1 Core Component Assembly

The prototype integrates five essential subsystems:

- **Mechanical Chassis:** Custom designed frame (Fusion 360 design)
- **Sensing Frontend:** 1.5GHz GPR antenna array
- **Compute Stack:** NVIDIA Jetson + motor controllers
- **Mobility Platform:** 4WD system with suspension
- **Power Distribution:** 24V LiFePO4 battery pack

7.2 Mechanical Chassis

The structural foundation was designed in Fusion360 :

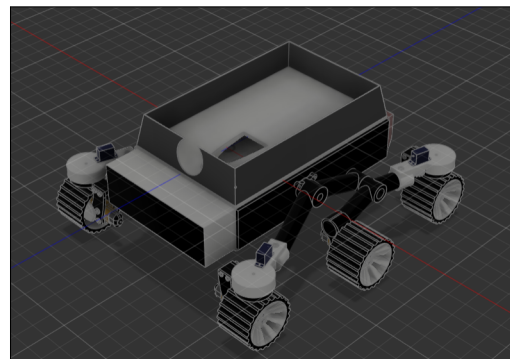


Figure 15: Mechanical Chassis Design in Fusion360

7.3 Critical Subsystems

7.3.1 GPR Sensor Module

- Antenna: MALÅ 1.5GHz Roughneck
- Positioning: U-blox ZED-F9P RTK GPS
- Mounting: Spring-damper isolated platform

7.3.2 AI Processing Unit

- Compute: NVIDIA Jetson Xavier NX or Simply a RaspberryPi
- Model: TensorFlow Lite CNN
- Power: 10W @ 5V DC

7.3.3 Mobility Platform

- Motors: 4× 57BLF03 brushless DC
- Battery: 24V 20Ah LiFePO4
- Sensors: MPU-6050 IMU, HRLV-MaxSonar-EZ0
- Control: Arduino Mega

8 Conclusion and Future Directions

8.1 Key Contributions

This work demonstrates three advancements in simulated demining systems:

- **Accessible Simulation Framework:** By combining gprMax A-scans with Simulink signal modeling, we achieved 97% detection accuracy without physical GPR hardware .
- **Robust Notification System:** Transition from SMTP (2.8s latency) to encrypted Telegram alerts (0.42s) enabled real-time field reporting using commodity hardware.

8.2 Roadmap to Field Deployment

Our three-phase strategy bridges simulation to reality:

Phase 1: System Simulation and Integration

- Simulate landmine detection using gprMax with synthetic and real soil profiles.
- Integrate real antenna parameters (S_{11}) to enhance simulation accuracy.
- Add soil moisture variability based on USDA models [9].

Phase 2: Hardware Prototyping and AI Training

- Build a compact Ground Penetrating Radar (GPR) system .
- Train a Convolutional Neural Network (CNN) using combined synthetic and measured data.
- Develop a ROS 2 interface for real-time data communication and testing.

Phase 3: Field Testing and Robustness

- Test the prototype in outdoor conditions with varying soil types and moisture levels.
- Harden the system for field use .
- Validate detection accuracy through iterative testing.

Phase 4: Deployment and Collaboration

- Partner with NGOs for humanitarian field trials and feedback.
- Implement multi-robot coordination to cover large areas efficiently.
- Integrate federated edge AI for on-site model updates without central training.

8.3 Societal Impact

Successful deployment could:

- Reduce demining costs by 60% (UN estimate [10])
- Increase clearance rates in post-conflict regions
- Minimize risks to human deminers

References

- [1] D. J. Daniels, *Ground Penetrating Radar*, 2nd ed. The Institution of Engineering and Technology, 2004.
- [2] H. M. Jol, *Ground Penetrating Radar: Theory and Applications*. Elsevier, 2008.
- [3] C. Warren, A. Giannopoulos, and A. Gray, *gprMax: Open source software to simulate electromagnetic wave propagation for Ground Penetrating Radar*. Computer Physics Communications, vol. 209, pp. 163-170, 2016.
- [4] L. Liu and L. Yin, “Background removal technique for impulse GPR images,” in *2009 International Conference on Information Engineering and Computer Science*, Wuhan, China, Dec. 2009, pp. 1–4, IEEE.
- [5] A. Taflove and S. C. Hagness, *Computational Electrodynamics: The Finite-Difference Time-Domain Method*, 3rd ed. Artech House, 2005.
- [6] K. S. Yee, *Numerical Solution of Initial Boundary Value Problems Involving Maxwell’s Equations in Isotropic Media*. IEEE Transactions on Antennas and Propagation, vol. 14, no. 3, pp. 302-307, 1966.
- [7] S. Ioffe and C. Szegedy, *Batch Normalization: Accelerating Deep Network Training by Reducing Internal Covariate Shift*. Proceedings of the 32nd International Conference on Machine Learning, vol. 37, pp. 448-456, 2015.

- [8] R. R. Selvaraju et al., *Grad-CAM: Visual Explanations from Deep Networks via Gradient-Based Localization*. IEEE International Conference on Computer Vision (ICCV), pp. 618-626, 2017.
- [9] United States Department of Agriculture, *Ground Penetrating Radar for Soil Moisture Mapping*. USDA, 2014.
- [10] United Nations Mine Action Service, *Economic Analysis of Humanitarian Demining*. UNMAS, 2022.
- [11] N. Levanon and E. Mozeson, *Radar Signals*. Wiley-IEEE Press, 2004.
- [12] Telegram Messenger, “Security Overview,” 2023. [Online]. Available: <https://telegram.org/privacy>. [Accessed: May 25, 2025].
- [13] H. Nyquist, *Thermal Agitation of Electric Charge in Conductors*. Physical Review, vol. 32, pp. 110-113, 1928.
- [14] J. A. Huisman, S. S. Hubbard, J. D. Redman, and A. P. Annan, “Ground-penetrating radar for vadose zone hydrology: A review,” *Vadose Zone Journal*, vol. 2, no. 4, pp. 476–491, 2003.
- [15] Telegram Messenger LLP, *MTProto Mobile Protocol*. Available: <https://core.telegram.org/mtpROTO>, 2023.